Supporting Information accompanying the manuscript "*In situ* studies of NO reduction by H_2 over Pt using surface X-ray diffraction and transmission electron microscopy"

S. B. Roobol[1,‡], W. G. Onderwaater[1,2], M. A. van Spronsen[1,±], F. Carla[2], O. Balmes[2,+], V. Navarro[1,×], S. Vendelbo[3], P. J. Kooyman[3,♯], C. F. Elkjær[4], S. Helveg[4], R. Felici[2], J. W. M. Frenken[1,†], and I. M. N. Groot[1,5*]

[1] *Huygens-Kamerlingh Onnes Laboratory, Leiden University, P.O. Box 9504, 2300 RA Leiden, The Netherlands*

[2] *European Synchrotron Radiation Facility, BP 220, F-38043 Grenoble Cedex 9, France*

[3] *Catalysis Engineering, Chemical Engineering Department, Delft University of Technology, Julianalaan 136, 2628 BL Delft, the Netherlands*

[4] *Haldor Topsøe A/S, Haldor Topsøes Allé 1, DK-2800 Kgs. Lyngby, Denmark*

[5] *Gorlaeus Laboratories, Leiden University, P.O. Box 9502, 2300 RA Leiden, The Netherlands*

[‡] *Current address: ASML Netherlands B.V., De Run 6501, 5504 DR Veldhoven, the Netherlands*

[±] *Current address: Department of Chemistry and Chemical Biology, Harvard University, Cambridge, Massachusetts 02138, United States*

[+] *Current address: MAX IV Laboratory, S-22594 Lund, Sweden*

[*] *Current address: TNO, P.O. Box 155, 2600 AD Delft, the Netherlands*

[♯] *Current address: Department of Chemical Engineering, University of Cape Town, Private Bag X3, Rondebosch 7701, South Africa and*

[†] *Current address: Advanced Research Center for Nanolithography, P.O. Box 41883, 1009 DB Amsterdam, the Netherlands*

(Dated: January 27, 2017)

I. *SPACETIME*: ANALYSIS SOFTWARE FOR MICROSCOPY DATA OF DYNAMICAL PROCESSES

With the continuing advancement of imaging techniques along the whole spectrum of photon-, electron-, ion- and scanning probe microscopes, it has become increasingly common to apply such techniques for real-time, *in situ* studies of dynamical systems. When analyzing data from such experiments it is essential to correlate the images to parameters that are changing during the experiment, either spontaneously or intentionally, e.g. partial pressures of reactants and products or temperature. Furthermore, it is important that the analysis of these different measurements is synchronized in time. For example, when observing an increase in catalyst activity at a certain time, it is extremely valuable to be able to analyze whether at exactly the same time, or shortly before or after, a change in structural morphology is observed. In this way, the structure-activity relationship of catalysts can be investigated. To this end, we have developed open source software called *Spacetime* to aid in the analysis of data sets from *in situ* microscopy studies. This tool was used for the analysis of the present work and is made freely available[1].

Spacetime aims to give a unified view on the spatial microscopy data together with any time-dependent parameters related to the dynamics of the system under investigation. It supports highly heterogeneous datasets, both in character (e.g. spatial data acquired in a single shot, spatial data acquired by a scanning technique, or purely time-dependent data) and in data format (ranging from standard image formats and plain text files to several vendor-specific formats or extensions). The emphasis is on browsing through datasets and searching for correlations to identify which subsets need to be analyzed using conventional image- or data analysis software. If desired, *Spacetime* exports the originally heterogeneous dataset into a simple homogeneous format for analysis using other tools.

Spacetime has a modular design and uses a separate module for each supported data format. The user typically selects two or more modules, and configures each of them by selecting the data files and possibly defining other settings. Each module has a specific way of presenting its data. Time-dependent quantities can be plotted in graphs, showing the values versus time, while microscopy images are displayed together with a marker indicating the acquisition time and duration. The modules share a single time axis, which can be presented as an absolute date and time, or in the form of the time relative to a user-defined

time origin. When necessary, the timing of individual modules can be adjusted to correct for an offset in time (time calibration) or propagation delays of a physical observable. The precision of the time axis is as accurate as 10 μs, even though many data formats have a time resolution of only 1 s.

Combined data can be exported to various raster and vector image formats, and can be animated and saved as a movie. For presentation purposes *Spacetime* features a split-screen presentation mode, where the projector shows the selected combination of experimental data while the control interface remains on the computer/laptop screen.

Spacetime has been written in Python, a general-purpose programming language that is becoming increasingly popular in the scientific community[2]. *Spacetime* uses various open-source libraries, including NumPy[3] (numerical computation), Matplotlib[4] (plotting), and the Enthought TraitsUI toolkit[5] (graphical user interface or GUI). This makes *Spacetime* fully platform-independent so that it runs on e.g. Windows, Linux, and Mac OS X.

The code is modular and easily extensible. The description of the GUI, the plotting logic and the data handling code are fully separated for each of the supported file formats. This means that when adding a new file format, only the actual file handling code has to be written; The plotting code and GUI can be reused from other modules. Similarly, there can be multiple different graph types for a single file format.

At the time of writing, the following file formats are supported: basic image formats (including PNG, JPEG, TIFF and BMP), basic plain text formats (CSV and tabulated), Leiden Probe Microscopy[6] Camera RAW files for scanning probe microscopy, Gatan DigitalMicrograph 3[7] (DM3) images and stacks for transmission electron microscopy, TVIPS[8] extensions for TIFF images for transmission electron microscopy, and various mass spectrometer formats from Pfeiffer Vacuum[9], Stanford Research Systems[10] and MKS Instruments[11].

Figure S1 shows a screen shot taken from *Spacetime* for a typical TEM experiment.

II. TEM EXPERIMENTS

The experiments have been performed using a surface micromachined nanoreactor[12,13]. We have employed the latest generation of these devices, integrated on a single die[14]. It consists of a ~ 0.5 μm deep gas channel etched in a silicon die, with electron-transparent windows that allow for *in situ* TEM measurements of metal particles in a gas environment

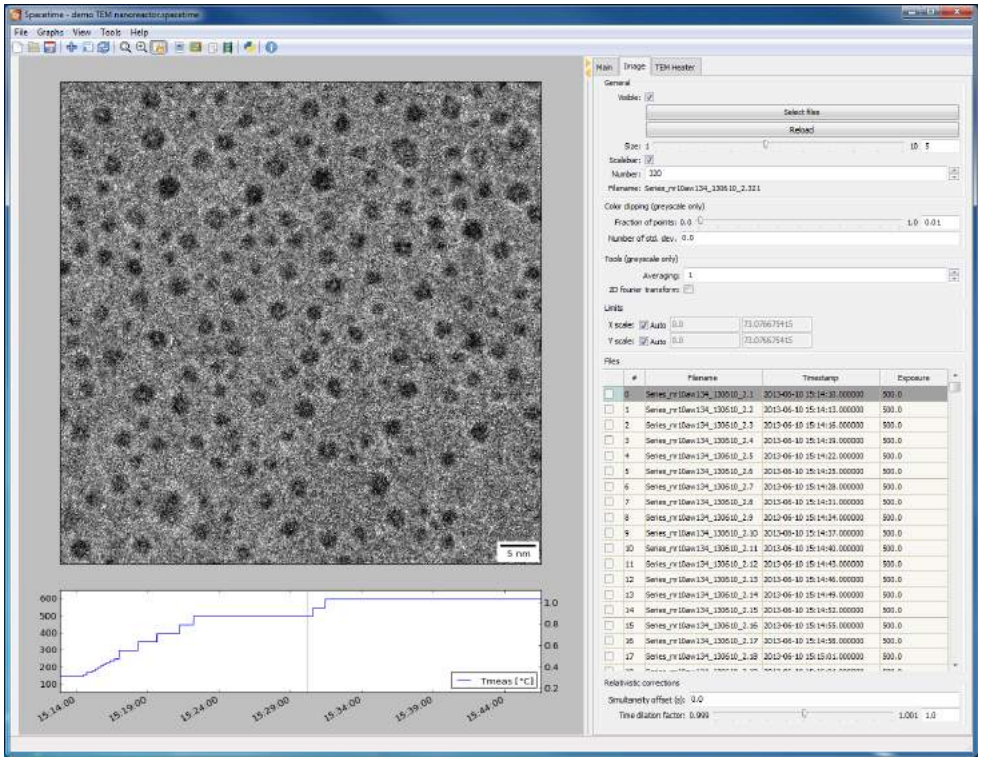

FIG. S1: An *in situ* TEM experiment with a screen shot from *Spacetime*. The left part of the window shows the experimental data, the right-hand panel allows detailed control over the display. The lower panel shows the trace of the sample temperature as a function of time, and the vertical line indicates the point in time at which the image was acquired. The gray band in this panel indicates the time window during which the image was recorded.

of more than 2 bar and up to 700°C. The electron-transparent windows consist of a 15 nm amorphous silicon nitride film. This film also coats the interior of the other parts of the channel to ensure chemical inertness. Two viton O-rings connect the gas channel to a pair of capillaries in a dedicated TEM sample holder. A molybdenum heater is embedded in the nanoreactor directly above the gas channel and heats a small region around the electron-transparent windows, while simultaneously measuring the temperature by use of a calibrated resistance measurement. The main differences between our specially manufactured nanoreactors and current commercially available systems are that our design minimizes gas dead volume and the heater area is wider than the gas channel, ensuring all gas entering the nanoreactor flows over a heated catalyst.

The nanoreactor is operated in a flow configuration, as used by Vendelbo et al.[15]. The

set-up is outlined in Fig. S2. Since the channel through the nanoreactor is extremely small (the reactor volume is 0.4 nl), the flow cannot be controlled by commercially available flow controllers. Instead, a certain gas pressure is set at the inlet, and the outlet is fed directly into a turbomolecular pump. To obtain a reasonable response time when changing the composition of the gas mixture, a gas flow is set up through a T-piece that is connected as close as possible to the inlet of the reactor and to a pressure regulator, backed by a vacuum pump. Most of the gas only flows through the T-piece and the pressure regulator, and only a small fraction flows through the reactor. The volume of the capillary between the T-piece and the reactor is large compared to the flow in this region, resulting in refresh times in the order of minutes. The gas stream is supplied by a gas mixing system[6,16] that allows composing mixtures of up to four gases plus a carrier gas at pressures up to 6 bar with a typical flow of 10 ml_n/min.

The outlet of the reactor is connected directly to a differentially pumped quadrupole mass spectrometer (T100 gas analyzer[6]). The pressure drops entirely over the length of the nanoreactor since the gas channel in the nanoreactor is small compared to the diameter of the capillaries leading to and from the nanoreactor. The geometry of the nanoreactor is fully symmetric so it is assumed that the pressure in the central region of the nanoreactor (where the windows and heater are located) is half the pressure at the inlet. Since all gas from the reactor is pumped into the mass spectrometer (via the differential-pumping stage), the sensitivity of the mass spectrometer is independent of the reactor pressure. The delay between an event in the reactor and detection by the mass spectrometer is approximately 30 s.

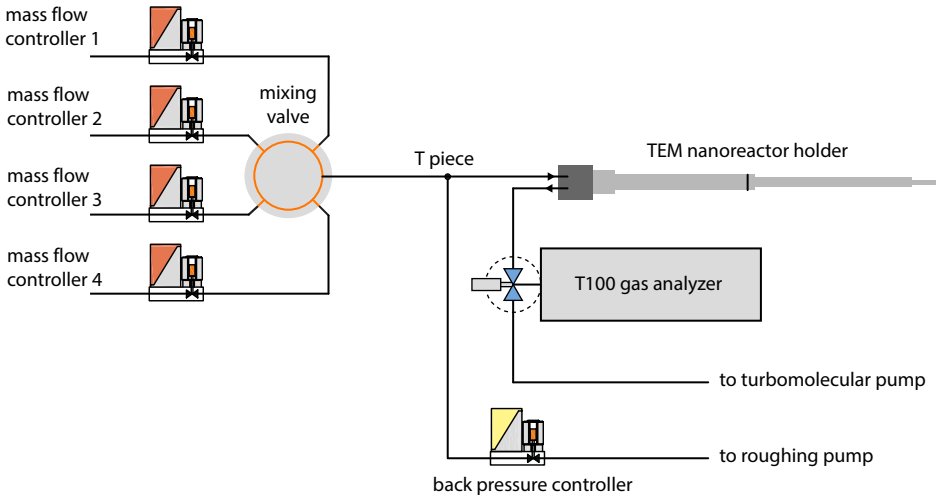

FIG. S2: Schematic of the gas system to operate the nanoreactor in a flow configuration. The main flow path leads from the mixing valve via the T-piece and the back pressure controller to the roughing pump. Only a small fraction flows from the T piece through the small nanoreactor channel and into the T100 analyzer.

III. PARTICLE SHAPE ANALYSIS

When exposing the platinum particles to varying ratios of NO and H_2, it became clear that it was desirable to quantify changes in particle shape. We have developed a new fitting method that quantifies the degree to which the corners of a faceted nanoparticle are rounded. This method does not rely on edge detection, contrary to other methods for analyzing TEM images of particles described in literature[15,17]. In those methods, the precise location of the contour of a particle is established, and a curve fitting procedure is used to obtain the optimal fit of a 1D curve in a 2D space. The weak element in these methods is the edge detection, which is a non-trivial operation, contrary to what is implied in these publications. In addition, the edge detection fails if the signal-to-noise ratio is low, as is the case in the dataset at hand in this paper. In this case, the low signal-to-noise ratio is caused by the electron-transparent windows of the nanoreactor that give a speckled background pattern, and by the low electron dose used, required to minimize beam effects. We use a least-squares optimization to fit a 2D simulated particle silhouette to a TEM image, thus avoiding edge detection completely.

We first describe the geometrical construction of the rounded polygon and then show how this is translated into a matrix of grayscale values on a discrete grid, matching the pixels of a TEM image.

The number of corners of the polygon N is assumed to be fixed and not a fit parameter. The degrees of freedom for the corner positions should be limited, e.g. to avoid concave polygons. Therefore it is assumed that all corners of the polygon are located on an ellipse, as is shown in Fig. S3a. The ellipse is described by two radii (a, b), the center coordinates (x_0, y_0), and an orientation angle ϕ of the major axis. The position of the corners can then be specified as a list of angles ($0 \leq \alpha_1 < ... < \alpha_N < 2\pi$).

In the absence of rounding, the polygon is simply formed by the N straight lines connecting neighboring corner points (Fig. S3b). Rounding is introduced via a single corner radius r for all N corners of the particle, as illustrated in Fig. S3c. The straight line segments then terminate at the tangent points to the inscribed circles at each corner. Next, the interior of the rounded polygon is filled (Fig. S3d). At this stage, the silhouette has sharp edges whereas the TEM images show edges that are somewhat blurred. This aspect needs to be taken into account. There is a second reason for blurring the sharp edge, namely to trans-

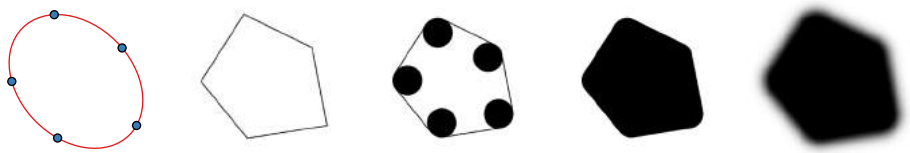

FIG. S3: Construction of a polygon on a discrete grid, having rounded corners and a fuzzy boundary. (a, b) The corner points are defined by polar coordinates with respect to the center of the ellipse. (c) The inscribed circle is drawn at every corner. (d) The interior is filled using a hole-filling algorithm. (e) The edges are drawn with a Gaussian intensity profile.

late the mathematical shape of Fig. S3d into a non-jagged grid representation that evolves continuously under variations in the corner position and corner rounding radius (even for variations smaller than the size of a pixel). For this purpose, we make the pixel grayscale values for pixels outside the silhouette drop off with the distance to the nearest point on the contour of the rounded polygon according to a Gaussian with a width σ (Fig. S3e). This approach ensures continuity of the least-squares error χ in all parameters when σ is not much smaller than the pixel size.

The result of Fig.S3e is scaled and an offset is added to match the background and foreground intensities of the TEM image. The entire procedure has $9 + N$ parameters and results in a least-squares error χ that is not only continuous but also differentiable with respect to these parameters, with the exception of the rounding radius parameter r, which clips at an upper limit depending on the particle size. This upper limit is given by the radius of the largest inscribed circle (at every corner) that fits within the enclosing polygon and this approximately matches the particle radius.

We use a least-squares optimization procedure based on a steepest-descent algorithm from Scipy[2]. Due to the low signal-to-noise ratio in the dataset in this paper, the procedure did not always converge to a shape that properly describes the particle, and manual tuning of the starting values was required. This can likely be improved by tailoring the optimization algorithm to this particle model and its choice of the parameters, but this has not been attempted. The fit procedure typically takes up to one minute on a 2.8 GHz Intel Core i7 CPU to converge for an image of 80×80 pixels.

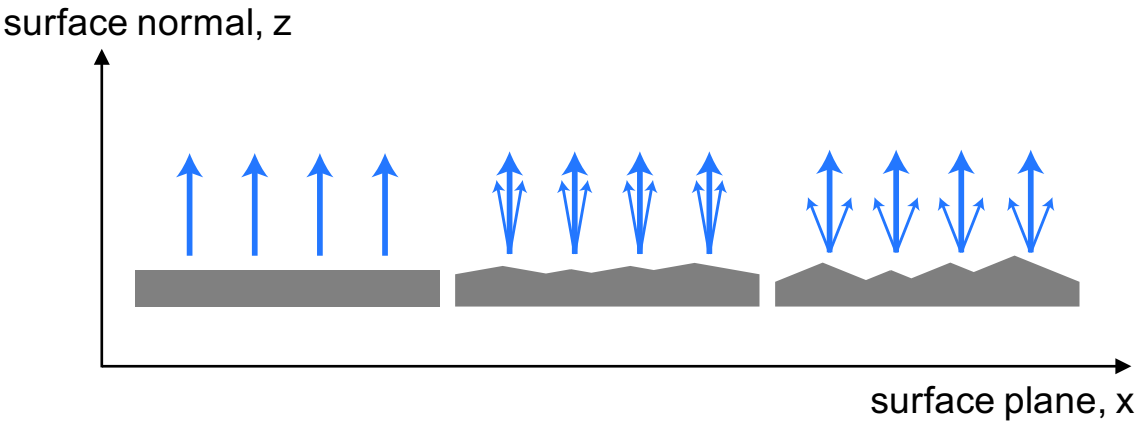

FIG. S4: The surface termination of a flat surface gives rise to crystal truncation rods (CTRs) along the surface normal (left-hand panel). The presence of facets on the surface results in the appearance of titled truncation rods (central and right-hand panel).

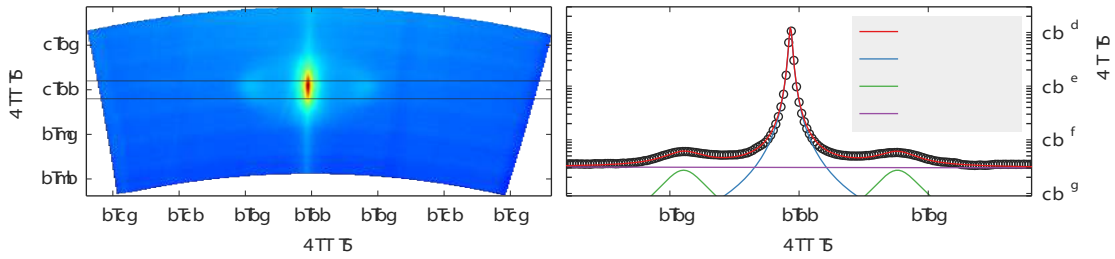

FIG. S5: The region indicated in the left-hand panel was used to further analyze the faceting. The position of the satellite peaks has been fitted using a least-squares optimization of three Lorentzian functions plus a sloped background. The satellite peaks were assumed to be symmetrically positioned on either side of the rod, and to have identical peak widths (right-hand panel).

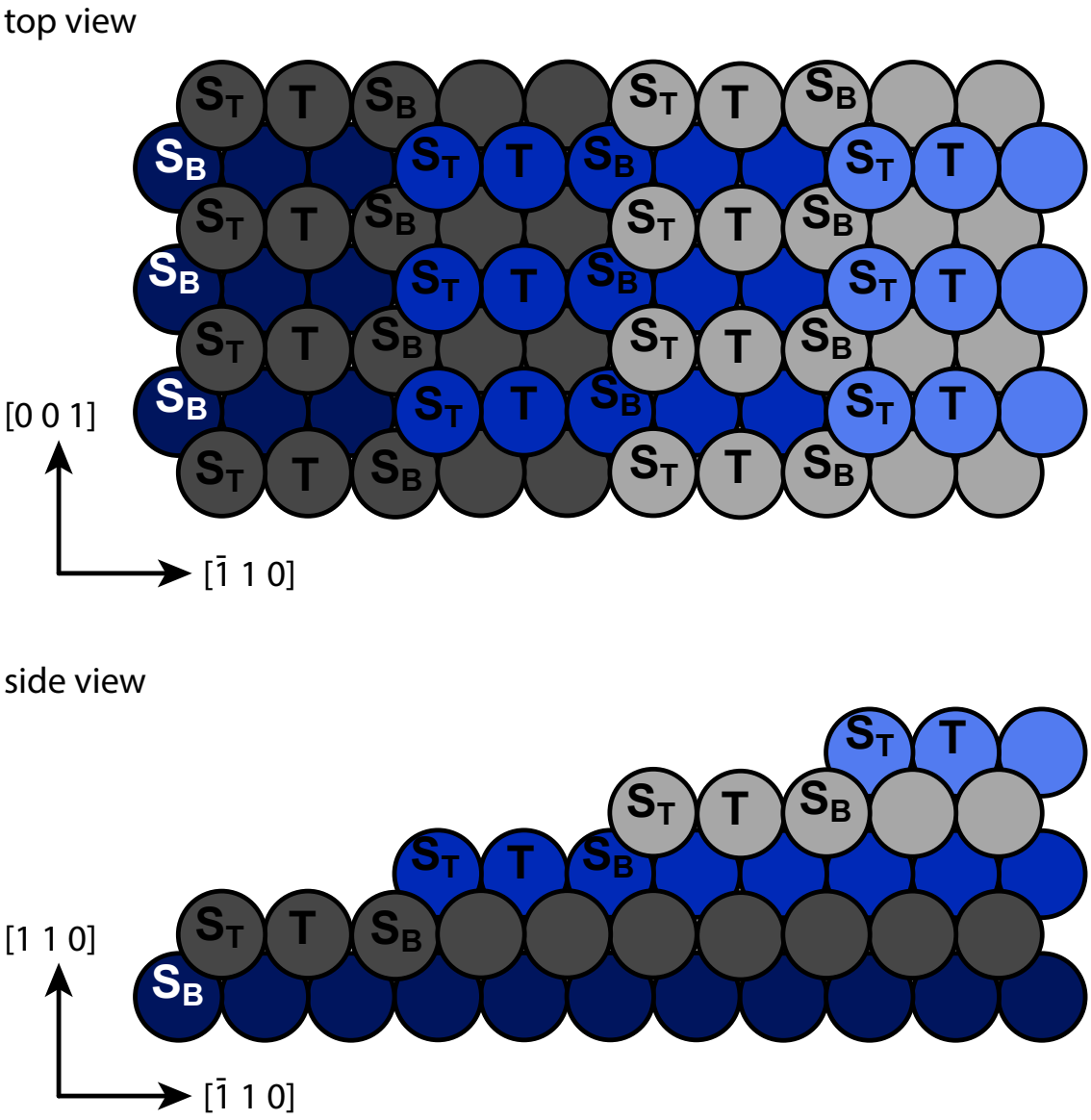

FIG. S6: Ball model of the stepped Pt(320) surface with its surface normal tilted 11.3° away from the [110] orientation. Atoms labeled with T are terrace atoms, atoms labeled with S_T are atoms at the top of the steps, and atoms labeled with S_B are atoms at the bottom of the steps.

---

* Electronic address: i.m.n.groot@lic.leidenuniv.nl

[1] *Spacetime*, URL http://spacetime.uithetblauw.nl/.

[2] F. Pérez, B. E. Granger, and J. D. Hunter, Computing in Science & Engineering **13**, 13 (2011).

[3] T. E. Oliphant, Computing in Science & Engineering **9**, 10 (2007).

[4] J. D. Hunter, Computing in Science & Engineering **9**, 90 (2007).

[5] *Enthought tools suite*, URL `http://www.enthought.com/`.

[6] *Leiden probe microscopy b.v.*, URL `http://www.leidenprobemicroscopy.com/`.

[7] *Gatan inc.*, URL `http://www.gatan.com/`.

[8] *Tvips gmbh*, URL `http://www.tvips.com/`.

[9] *Pfeiffer vacuum gmbh*, URL `http://www.pfeiffer-vacuum.com/`.

[10] *Stanford research systems*, URL `http://www.thinksrs.com/`.

[11] *Mks instruments*, URL `http://www.mksinstr.com/`.

[12] J. F. Creemer, S. Helveg, G. H. Hoveling, S. Ullmann, A. M. Molenbroek, P. M. Sarro, and H. W. Zandbergen, Ultramicroscopy **108**, 993 (2008).

[13] J. F. Creemer, S. Helveg, P. J. Kooyman, A. M. Molenbroek, H. W. Zandbergen, and P. M. Sarro, Journal of Microelectromechanical Systems **19**, 254 (2010).

[14] J. F. Creemer, F. Santagata, B. Morana, L. Mele, T. Alan, E. Iervolino, G. Pandraud, and P. M. Sarro, Proceedings of the IEEE 24th International Conference on Micro Electro Mechanical Systems p. 1103 (2011).

[15] S. B. Vendelbo, C. F. Elkjær, H. Falsig, I. Puspitasari, P. Dona, L. Mele, B. Morana, B. J. Nelissen, R. van Rijn, J. F. Creemer, et al., Nature Materials **13**, 884 (2014).

[16] C. T. Herbschleb, P. C. van der Tuijn, S. B. Roobol, V. Navarro, J. W. Bakker, Q. Liu, D. Stoltz, M. E. Cañas-Ventura, G. Verdoes, M. A. van Spronsen, et al., Review of Scientific Instruments **85**, 083703 (2014).

[17] H. Yoshida, K. Matsuura, Y. Kuwauchi, H. Kohno, S. Shimada, M. Haruta, and S. Takeda, Applied Physics Express **4**, 065001 (2011).